The Influence of Defects on the Electron-Transfer and Magnetic Properties of $Rb_xMn[Fe(CN)_6]_y \cdot zH_2O$

Esther J. M. Vertelman,[†,‡] Enrico Maccallini,[†,§] Dimitris Gournis,[†] Petra Rudolf,[†] Thomas Bakas,[⊥] Javier Luzon,[†] Ria Broer,[†] Audrius Pugzlys,[†] Tom T. A. Lummen,[†] Paul H. M. van Loosdrecht,[†] and Petra J. van Koningsbruggen*[,†,‡]

Materials Science Centre and Stratingh Institute of Chemistry and Chemical Engineering, University of Groningen, Nijenborgh 4, 9747 AG Groningen, The Netherlands, Department of Physics, University of Calabria, via P. Bucci, 87036 Arcavacata di Rende, Italy, and Department of Physics, University of Ioannina, 45110 Ioannina, Greece

Received November 15, 2005. Revised Manuscript Received February 7, 2006

The synthesis and detailed characterization of a few samples of the compound $Rb_xMn[Fe(CN)_6]_y \cdot zH_2O$ are described. The composition of the materials significantly depends on the applied preparative conditions. Analysis of spectroscopic results (FTIR, Raman, ^{57}Fe Mössbauer, XPS) and X-ray powder-diffraction data yielded a further assessment of the difference in structural features in terms of the amount of $Fe(CN)_6$ vacancies and the associated number of water molecules. The characteristic individual magnetic behavior, as well as the metal-to-metal charge-transfer capabilities of the various samples, could be related to significant changes within the structures that appear to be associated with the synthetic method used.

Introduction

A new challenge in the field of molecular magnetism is the design of optically switchable magnetic materials. Several types of solid-state photomagnetic switches have been reported that differ in the mechanism by which specific electronic features of the metal ion are optically manipulated. Examples are represented by (i) light-induced excited spin-state trapping (LIESST), which involves reversible switching between spin states of Fe^{II} [1−4] or Fe^{III} spin crossover compounds,[5−7] (ii) ligand-driven light-induced spin-change (LD-LISC), in which photoisomerization of, for example, a stilbenoid ligand triggers the spin crossover of an Fe^{II} [8−11] or Fe^{III} center,[10,12] (iii) metal-to-ligand charge-transfer promoted by light irradiation in valence tautomeric systems such as nitroprusside[13−16] and Co^{II} [17−22] or Mn^{II} semiquinone complexes.[20,23]

Another type of switchable magnetic material is represented by various types of heterobimetallic Prussian Blue (PB) analogues, in which the interplay between the two different adjacent metal ions is crucial for the observation of photoinduced phenomena. The first example of this effect has been reported for $K_{0.2}Co_{1.4}[Fe(CN)_6] \cdot 6.9H_2O$,[24−28] for which an entirely reversible metal-to-metal charge transfer

* To whom correspondence should be addressed. E-mail: P.J.van.Koningsbruggen@rug.nl. Tel.: 31-50-3634363. Fax: 31-50-3634315.
† Materials Science Centre, University of Groningen.
‡ Stratingh Institute of Chemistry and Chemical Engineering, University of Groningen.
§ University of Calabria.
⊥ University of Ioannina.

(1) Decurtins, S.; Gütlich, P.; Kohler, C. P.; Spiering, H.; Hauser, A. *Chem. Phys. Lett.* **1984**, *105*, 1.
(2) Decurtins, S.; Gütlich, P.; Kohler, C. P.; Spiering, H. *Chem. Commun.* **1985**, 430.
(3) Hauser, A. *J. Chem. Phys.* **1991**, *94*, 2741.
(4) Hauser, A. In *Spin Crossover in Transition Metal Compounds II*; Gütlich, P., Goodwin, H. A., Eds.; *Top. Curr. Chem.* **2004**, *234*, 155.
(5) Hayami, S.; Gu, Z. Z.; Shiro, M.; Einaga, Y.; Fujishima, A.; Sato, O. *J. Am. Chem. Soc.* **2000**, *122*, 7126.
(6) Juhasz, G.; Hayami, S.; Sato, O.; Maeda, Y. *Chem. Phys. Lett.* **2002**, *364*, 164.
(7) Hayami, S.; Hashiguchi, K.; Inoue, K.; Maeda, Y. *J. Nucl. Radiochem. Soc.* **2004**, *5*, N1.
(8) Boillot, M.-L.; Roux, C.; Audiere, J.-P.; Dausse, A.; Zarembowitch, J. *Inorg. Chem.* **1996**, *35*, 3975.
(9) Boillot, M.-L.; Chantraine, S.; Zarembowitch, J.; Lallemand, J.-Y.; Prunet, J. *New J. Chem.* **1999**, 179.
(10) Boillot, M.-L.; Zarembowitch, J.; Sour, A. In *Spin Crossover in Transition Metal Compounds II*; Gütlich, P., Goodwin, H. A., Eds.; *Top. Curr. Chem.* **2004**, *234*, 261.
(11) Roux, C.; Zarembowitch, J.; Gallois, B.; Granier, T.; Claude, R. *Inorg. Chem.* **1994**, *33*, 2273.
(12) Sour, A.; Boillot, M.-L.; Riviere, E.; Lesot, P. *Eur. J. Inorg. Chem.* **1999**, 2117.
(13) Carducci, M. D.; Pressprich, M. R.; Coppens, P. *J. Am. Chem. Soc.* **1997**, *119*, 2669.
(14) Coppens, P.; Fomitchev, D. V.; Carducci, M. D.; Culp, K. *J. Chem. Soc., Dalton Trans.* **1998**, 865.
(15) Gu, Z. Z.; Sato, O.; Iyoda, T.; Hashimoto, K.; Fujishima, A. *J. Phys. Chem.* **1996**, *100*, 18289.
(16) Schaniel, D.; Schefer, J.; Imlau, M.; Woike, T. *Phys. Rev. B* **2003**, *68*, 104108.
(17) Carbonera, C.; Dei, A.; Letard, J.-F.; Sangregorio, C.; Sorace, L. *Angew. Chem., Int. Ed.* **2004**, *43*, 3136.
(18) Carbonera, C.; Dei, A.; Sangregorio, C.; Sorace, L. *Chem. Phys. Lett.* **2004**, *396*, 198.
(19) Dei, A.; Gatteschi, D.; Sangregorio, C.; Sorace, L. *Acc. Chem. Res.* **2004**, *37*, 827.
(20) Hendrickson, D. N.; Pierpont, C. G. In *Spin Crossover in Transition Metal Compounds II*; Gütlich, P., Goodwin, H. A., Eds.: *Top. Curr. Chem.* **2004**, *234*, 63.
(21) Neuwahl, F. V. R.; Righini, R.; Dei, A. *Chem. Phys. Lett.* **2002**, *352*, 408.
(22) Sato, O.; Hayami, S.; Gu, Z. Z.; Seki, K.; Nakajima, R.; Fujishima, A. *Chem. Lett.* **2001**, 874.
(23) Caneschi, A.; Dei, A. *Angew. Chem., Int. Ed.* **1998**, *37*, 3005.
(24) Sato, O.; Iyoda, T.; Fujishima, A.; Hashimoto, K. *Science* **1996**, *272*, 704.
(25) Verdaguer, M. *Science* **1996**, *272*, 698.
(26) Dei, A. *Angew. Chem., Int. Ed.* **2005**, *44*, 1160.
(27) Sato, O. *Acc. Chem. Res.* **2003**, *36*, 692.
(28) Verdaguer, M.; Bleuzen, A.; Marvaud, V.; Vaisserman, J.; Seuleiman, M.; Desplanches, C.; Scuiller, A.; Train, A.; Garde, R.; Gelly, G.; Lomenech, C.; Rosenman, I.; Veillet, P.; Cartier, C.; Villain, F. *Coord. Chem. Rev.* **1999**, *190−192*, 1023.

10.1021/cm052521x CCC: $33.50
Published on Web 03/02/2006

induced by photons of different energies resulted in an unprecedented reversible transition from a diamagnetic to a ferrimagnetically ordered state. The magnetization of the material could be repeatedly raised and decreased by alternating irradiation with red and blue light carried out below the ordering temperature of the ferrimagnetic $Co^{II}-Fe^{III}$ phase, i.e., 20 K. It has been anticipated that the magnetic and optical properties of this material may not be controlled only by (i) light-excitation, but also by (ii) electrostatic pressure or (iii) (electro)chemical methods.[29,30] Very significant advances in the field, possible applications in particular, include the observation of switching behavior at room temperature by applying external hydrostatic pressure[31,32] or light-irradiation.[33−35] Moreover, it appears that the photoinduced magnetic phenomena within the family of heterobimetallic PB analogues are not limited to the Co−Fe combination. In fact, literature reports a few examples of alternatives, such as $Cu^{II}-Mo^{IV} \leftrightarrow Cu^{I}-Mo^{V}$,[36−38] $W^{IV}-Co^{III} \leftrightarrow W^{V}-Co^{II}$,[39] and $Mn^{III}-Fe^{II} \leftrightarrow Mn^{II}-Fe^{III}$.[40]

Our research was triggered by the intriguing results reported on $RbMn[Fe(CN)_6]$.[32,41−48] At room temperature, the material contains high-spin Mn^{II} ($S = 5/2$) and low-spin Fe^{III} ($S = 1/2$), whereas cooling of the compound induces a structural phase transition associated with a charge transfer[48] that yields high-spin Mn^{III} ($S = 2$) and low-spin Fe^{II} ($S = 0$) and results in a ferromagnetic ordering below $T_C = 12$ K. A similar process has also been found to be induced by light at 3 K,[45] and there is an indication that it can also be triggered by X-ray illumination of 14.575 keV.[49]

$RbMn[Fe(CN)_6]$ represents an appealing object for further study aimed at the exploration of its potential for applications in molecular electronics. A vital advantageous criterion supporting this is the possibility of reaching a maximal photoefficiency, which is a corollary of its fairly stoichiometric Mn:Fe ratio. This is in fact a drawback of the family of related nonstoichiometric $Co^{III}-Fe^{II}$ PB analogues,[25,50−54] for which the volume changes accompanying the charge transfer require a flexibility of the 3D network generated by Fe defects, thus preventing the optimization of the quantum yield by restricting the number of photoactive Co−Fe pairs.

This contribution focuses on acquiring a more-detailed insight into the relationship between structural features and metal-to-metal charge-transfer capabilities of $Rb_xMn[Fe(CN)_6]_y \cdot zH_2O$ analogues. It is shown in which way small variations in the synthetic procedures may give rise to materials that differ considerably in composition and physical behavior. A novel aspect of this study concerns the use of ^{57}Fe Mössbauer spectroscopy and XPS measurements for the characterization of the obtained materials. In the future, the knowledge acquired from this work may be further exploited for the targeted design of PB compounds with predetermined, optimized physical properties.

Experimental Section

Synthesis. All chemicals were purchased from Sigma-Aldrich and used without further purification.

Sample 1 was prepared by slowly adding (addition time: 20 min) an aqueous solution (50 mL) containing $K_3Fe(CN)_6$ (0.1 M) and RbCl (1 M) to an aqueous solution (50 mL) containing $MnCl_2 \cdot 4H_2O$ (0.1 M).

Sample 2 was prepared by slowly adding (addition time: 20 min) an aqueous solution (50 mL) containing $MnCl_2 \cdot 4H_2O$ (0.1 M) to an aqueous solution (50 mL) containing $K_3Fe(CN)_6$ (0.1 M) and RbCl (1 M).

Sample 3 was prepared by simultaneously adding equal amounts of an aqueous solution (50 mL) containing $MnCl_2 \cdot 4H_2O$ (0.1 M) and an aqueous solution (50 mL) containing both $K_3Fe(CN)_6$ (0.1 M) and RbCl (1 M) together over a period of 5 h.

Sample 4 was prepared in a manner similar to that for sample 2, but its complete synthesis took place in the dark. Characterization of this sample took place in daylight (except for the XPS measurements, for which the sample was shielded from all light except the X-rays).

All solutions were stirred mechanically and kept at a temperature of 50 °C during the addition procedure and over a successive hour. A brown powder precipitated; this was centrifuged and washed

(29) Bleuzen, A.; Escax, V.; Itie, J. P.; Munsch, P.; Verdaguer, M. *C. R. Chim.* **2003**, *6*, 343.
(30) Shimamoto, N.; Ohkoshi, S.-I.; Sato, O.; Hashimoto, K. *Inorg. Chem.* **2002**, *41*, 678.
(31) Ksenofontov, V.; Levchenko, G.; Reiman, S.; Gütlich, P.; Bleuzen, A.; Escax, V.; Verdaguer, M. *Phys. Rev. B* **2003**, *68*, 024415.
(32) Moritomo, Y.; Hanawa, M.; Ohishi, Y.; Kato, K.; Takata, M.; Kuriki, A.; Nishibori, E.; Sakata, M.; Ohkoshi, S.-I.; Tokoro, H.; Hashimoto, K. *Phys. Rev. B* **2003**, *68*, 144106.
(33) Kamiya, M.; Hanawa, M.; Moritomo, Y.; Isobe, Y.; Tateishi, J.; Kato, K.; Nakamura, A. *Phys. Rev. B* **2004**, *69*, 052102.
(34) Liu, H. W.; Matsuda, T.; Gu, Z. Z.; Takahashi, K.; Cui, A. L.; Nakajima, R.; Fujishima, A.; Sato, O. *Phys. Rev. Lett.* **2003**, *90*, 167403.
(35) Shimamoto, N.; Ohkoshi, S.-I.; Sato, O.; Hashimoto, K. *Chem. Lett.* **2002**, 486.
(36) Ohkoshi, S.-I.; Machida, N.; Zhong, Z. J.; Hashimoto, K. *Synth. Met.* **2001**, *122*, 523.
(37) Rombaut, G.; Verelst, M.; Golhen, S.; Ouahab, L.; Mathoniere, C.; Kahn, O. *Inorg. Chem.* **2001**, *40*, 1151.
(38) Mathoniere, C.; Podgajny, R.; Guionneau, P.; Labrugere, C.; Sieklucka, B. *Chem. Mater.* **2005**, *17*, 442.
(39) Arimoto, Y.; Ohkoshi, S.-I.; Zhong, Z. J.; Seino, H.; Mizobe, Y.; Hashimoto, K. *J. Am. Chem. Soc.* **2003**, *125*, 9240.
(40) Ohkoshi, S.-I.; Tokoro, H.; Hashimoto, K. *Coord.Chem.Rev.* **2005**, *249*, 1830 and references therein.
(41) Ohkoshi, S.-I.; Tokoro, H.; Utsunomiya, M.; Mizuno, M.; Abe, M.; Hashimoto, K. *J. Phys. Chem. B* **2002**, *106*, 2423.
(42) Moritomo, Y.; Kato, K.; Kuriki, A.; Takata, M.; Sakata, M.; Tokoro, H.; Ohkoshi, S.-I.; Hashimoto, K. *J. Phys. Soc. Jpn.* **2002**, *71*, 2078.
(43) Kato, K.; Morimoto, Y.; Takata, M.; Sakata, M.; Umekawa, M.; Hamada, N.; Ohkoshi, S.-I.; Tokoro, H.; Hashimoto, K. *Phys. Rev. Lett.* **2003**, *91*, 25502.
(44) Moritomo, Y.; Kuriki, A.; Ohoyama, K.; Tokoro, H.; Ohkoshi, S.-I.; Hashimoto, K.; Hamada, N. *J. Phys. Soc. Jpn.* **2003**, *72*, 456.
(45) Tokoro, H.; Ohkoshi, S.-I.; Hashimoto, K. *Appl. Phys. Lett.* **2003**, *82*, 1245.
(46) Tokoro, H.; Ohkoshi, S.-I.; Matsuda, T.; Hashimoto, K. *Inorg. Chem.* **2004**, *43*, 5231.
(47) Ohkoshi, S.-I.; Matsuda, T.; Tokoro, H.; Hashimoto, K. *Chem. Mater.* **2005**, *17*, 81.
(48) Moritomo, Y.; Kato, K.; Kuriki, A.; Takata, M.; Sakata, M.; Tokoro, H.; Ohkoshi, S.-I.; Hashimoto, K. *J. Phys. Soc. Jpn.* **2003**, *72*, 2698.
(49) Margadonna, S.; Prassides, K.; Fitch, A. N. *Angew. Chem,. Int. Ed.* **2004**, *43*, 6316.
(50) Sato, O.; Iyoda, T.; Fujishima, A.; Hashimoto, K. *Science* **1996**, *271*, 49.
(51) Bleuzen, A.; Lomenech, C.; Escax, V.; Villain, F.; Varret, F.; Cartier dit Moulin, C.; Verdaguer, M. *J. Am. Chem. Soc.* **2000**, *122*, 6648.
(52) Cartier dit Moulin, C.; Villain, F.; Bleuzen, A.; Arrio, M.-A.; Sainctavit, P.; Lomenech, C.; Escax, V.; Baudelet, F.; Dartyge, E.; Gallet, J.-J.; Verdaguer, M. *J. Am. Chem. Soc.* **2000**, *122*, 6653.
(53) Escax, V.; Bleuzen, A.; Cartier dit Moulin, C.; Villain, F.; Goujon, A.; Varret, F.; Verdaguer, M. *J. Am. Chem. Soc.* **2001**, *123*, 12536.
(54) Champion, G.; Escax, V.; Cartier dit Moulin, C.; Bleuzen, A.; Villain, F.; Baudelet, F.; Dartyge, E.; Verdaguer, M. *J. Am. Chem. Soc.* **2001**, *123*, 12544.

Table 1. Analytical Data for $Rb_xMn[Fe(CN)_6]_y \cdot zH_2O$[a]

sample	% Rb	% Mn	% Fe	% C	% N	% H	calcd composition
1_{obs}	14.96	16.42	14.31	18.91	21.28	1.44	$Rb_{0.59}Mn[Fe(CN)_6]_{0.86} \cdot 2.63H_2O$
1_{calcd}	14.96	16.42	14.35	18.52	21.59	1.58	
2_{obs}	22.24	15.51	15.20	20.00	22.61	0.25	$Rb_{0.92}Mn[Fe(CN)_6]_{0.95} \cdot 1.03H_2O$
2_{calcd}	22.24	15.51	15.02	19.38	22.61	0.59	
3_{obs}	22.75	15.09	15.04	20.19	22.89	0.18	$Rb_{0.97}Mn[Fe(CN)_6]_{0.98} \cdot 1.03H_2O$
3_{calcd}	22.75	15.08	15.04	19.41	22.63	0.57	
4_{obs}	19.97	15.83	14.96	19.64	22.40	0.67	$Rb_{0.81}Mn[Fe(CN)_6]_{0.95} \cdot 1.24H_2O$
4_{calcd}	19.97	15.83	15.22	19.64	22.90	0.72	

[a] The error in the observed percentages is ±0.3%.

twice with distilled water at room temperature. The powder was allowed to dry in air for about 12 h at room temperature. Yield (on the basis of Mn): 96% (sample 1), 86% (sample 2), 82% (sample 3), and 84% (sample 4).

Instrumentation and Measurement. *Elemental Analysis.* Elemental analysis of Rb, Mn, Fe (inductive coupling plasma atomic emission spectroscopy after demineralization in H_2SO_4/HNO_3), C, H (combustion above 850 °C and then IR detection), and N (combustion above 850 °C and then quantogravimetry) was performed at the analysis facility of CNRS in Vernaison, France. The O atom was presumed to be the only other element present and obtained by difference to 100%.

X-ray Powder Diffraction. X-ray powder-diffraction patterns were recorded at room temperature on a Philips PW 1830 diffractometer using ~0.5 g of carefully grinded powder. The radiation was Cu α_1 and α_2, and a monochromator was used to reduce the β radiation. The 2θ range was 10−60°, with a step size of 0.02° and 2 s per step. The receiving slit had a width of 1°. The spectra were then refined with a Rietveld structure refinement program (TOPAS[55]), using both the high- ($F\bar{4}3m$) and low-temperature phase ($I\bar{4}m2$), as found by Kato et al.[43] and Moritomo et al.[42]

FTIR Spectra. Spectra were recorded at room temperature on a Galaxy series FTIR by Mattson Instruments using KBr-mulled tablets. The spectral resolution was 2 cm^{-1}.

Raman Spectra. Room-temperature polarized Raman scattering measurements in the spectral region 2000−2300 cm^{-1} were performed in a backscattering configuration, using a micro-Raman spectrometer (T64000 Jobin Yvon) that consisted of a double grating monochromator acting as a spectral filter and a polychromator that dispersed the scattered light on a liquid-nitrogen-cooled CCD. The spectral resolution of the experiments was higher than 1 cm^{-1}. The second harmonic of a Nd:YVO_4 laser (532 nm; Verdi−Coherent) was used as a light source. A portion of the laser output (0.2 mW) was focused on the sample using a 50× microscope objective. The power density on the sample was on the order of 10 W/m^2. A study of photostability of the samples revealed that at excitation densities above 100 W/m^2, a darkening of the irradiated spot takes place, which indicates photoinduced changes. In the case of 10 times lower excitation density, i.e., 10 W/m^2, Raman spectra measured on the same spot are stable at room temperature and there are no noticeable differences between spectra recorded at different spots.

^{57}Fe Mössbauer Spectroscopy. Mössbauer spectra were collected at 80 K in an exchange gas cryostat. A conventional constant-acceleration spectrometer was used, equipped with a ^{57}Co/Rh source kept at room temperature and calibrated with Fe metal. Isomer shift values are reported relative to iron metal (α-Fe). The spectra were fitted on a PC with a least-squares minimization procedure assuming Lorentzian line shapes.

Magnetic Measurements. Magnetic measurements were performed on a Quantum Design magnetometer with a superconducting quantum interference device. The sample was prepared by putting 20−30 mg of the compound (accurately weighed) between two pieces of cotton wool in a gelcap. In the magnetic susceptibility measurements, the sample was first slowly cooled from room temperature to 5 K. The field was then kept constant at 0.1 T while the temperature was varied from 5 to 350 K and back to 150 K. The inverse magnetic susceptibility data were fitted with a straight line. From the fit, we calculated the Curie constant (C) and the Curie−Weiss temperature (θ) via the formula $\chi_M = C/(T - \theta)$, where χ_M = molar magnetic susceptibility and T = temperature.

In the magnetization measurements, the temperature was first varied from 5 to 20 K in the absence of a magnetic field (zero-field cooling, ZFC); the field was then kept constant at 0.01 T and the temperature was varied from 20 to 5 K (field cooling, FC). Finally, the field was switched off again and the temperature was varied from 5 to 20 K (remanence).

X-ray Photoelectron Spectroscopy (XPS). For the XPS measurements, we used evaporated gold films supported on glass as substrates. They were cleaned in an ozone discharge (UV−ozone photoreactor TM PR100, Ultra Violet Products) for 15 min and sonicated in ethanol for 15 min immediately before being employed. Prussian Blue analogue powder samples were dispersed in distilled−deionized water and after being stirred for 15 min, a small drop of the suspension was left to dry in air on the substrate.

The samples were introduced through a load look system into an SSX-100 (Surface Science Instruments) photoelectron spectrometer with a monochromatic Al Kα X-ray source ($h\nu$ = 1486.6 eV). The base pressure in the spectrometer during the measurements was 1×10^{-9} Torr. The photoelectron takeoff angle was 37°. The energy resolution was set to 1.4 eV. Sample charging was compensated for by directing an electron flood gun supplying 0.1 eV kinetic energy electrons onto the sample and covering the sample holder with a Au grid. XPS binding energies were referenced to the nitrogen signal at 398 eV (cyanide groups).[56,57] The XP spectra showed no X-ray induced changes. Spectral analysis included Shirley or Tougaard background subtraction and peak deconvolution that employed Gaussian functions in a least-squares curve-fitting program (WinSpec) developed at the LISE, University of Namur, Belgium.

Results and Discussion

General. Analytical data for the $Rb_xMn[Fe(CN)_6]_y \cdot zH_2O$ compounds are compiled in Table 1. Contrary to the materials reported by the group of Ohkoshi and Hashimoto,[32,40−44,46,58−61]

(55) *TOPAS: General Profile Analysis Software for Powder Diffraction Data*, version 2; Bruker AXS: Karlsruhe, Germany, 2000.

(56) Cataldi, T. R. I.; De Benedetto, G. E.; Bianchini, A. *J. Electroanal. Chem.* **1998**, *448*, 111.
(57) Yatsimirskii, K. B.; Nemoshkalenko, V. V.; Nazarenko, Y. *J. Electron Spectrosc. Relat. Phenom.* **1977**, *10*, 239.
(58) Yokoyama, T.; Tokoro, H.; Ohkoshi, S.-I.; Hashimoto, K.; Okamoto, K.; Ohta, T. *Phys. Rev. B* **2002**, *66*, 184111−1.

for which no specific details of the synthetic procedure were given, the samples under discussion here unambiguously appear to be hydrated and the composition is nonstoichiometric. The deviation from the perfect Rb:Mn:Fe stoichiometry of 1:1:1 for $Rb_xMn[Fe(CN)_6]_y \cdot zH_2O$ directly correlates with the lattice water content of the samples. Apart from the exclusion of daylight, the synthetic procedures for sample 2 and 4 were kept as similar as possible; however, a difference in the stoichiometry of the two samples is noted. In the course of our research, numerous samples have been synthesized and characterized. Apparently, stable compounds are formed that preferably contain close to 1 or 2.6 water molecules per Mn ion. This contribution will focus only on four representative samples originating from four different preparation methods. Reproduction of the synthesis has been carried out several times and the obtained products of the various synthetic routes appeared to have a reproducible physical behavior.

X-ray Powder Diffraction. An assessment of the phases present within the samples has been made by analyzing the X-ray powder diffraction patterns recorded at room temperature. For all samples, these show Bragg reflections characteristic for both the low-temperature phase (LT; tetragonal space group $I\bar{4}m2$, $Z = 2$) and the high-temperature phase (HT; cubic space group $F\bar{4}3m$, $Z = 4$). In the following, we will explicitly use the word "phase" when referring to a pure form of the material in either its $Mn^{II}-Fe^{III}$ or $Mn^{III}-Fe^{II}$ form, whereas the word "configuration" will be applied when dealing with a material in which fractions of both the $Mn^{II}-Fe^{III}$ and $Mn^{III}-Fe^{III}$ form are present.

Interpretation of the diffraction profiles of these mixed-phases was made on the basis of the results reported for synchrotron-radiation X-ray powder-diffraction studies performed at temperatures where $RbMn[Fe(CN)_6]$[42] and $Rb_{0.7}Mn_{1.15}[Fe(CN)_6]\cdot 2H_2O$[49] are present as single-phase materials. The X-ray diffraction data of $RbMn[Fe(CN)_6]$ could be interpreted for the low-temperature phase at 120 K ($I\bar{4}m2$) and for the high-temperature phase ($F\bar{4}3m$) at 240 K.[42] The evolution from the HT to LT phase involves the elongation of one of the cubic axes, resulting in a tetragonal space group with a concomitant reduction of the number of asymmetric units present in the unit cell from $Z = 4$ to $Z = 2$. For $Rb_{0.7}Mn_{1.15}[Fe(CN)_6]\cdot 2H_2O$, the X-ray powder-diffraction study was carried out at 295 K, and the data could be analyzed using the cubic $Fm\bar{3}m$ space group with $Z = 4$ for modeling the HT phase.[49] In fact, the HT space groups used in both studies differ only in that the 4-fold symmetry axis in $F\bar{4}3m$ is replaced by a mirror plane in $Fm\bar{3}m$; this implies that in the $Fm\bar{3}m$ HT phase, only one atomic position for Rb^+ is taken into account, whereas in the $F\bar{4}3m$ HT phase, two individual Rb^+ sites exist.

In the Rietveld structure refinement procedure (TOPAS[55]) used to analyze the X-ray diffraction patterns of the present $Rb_xMn[Fe(CN)_6]_y\cdot zH_2O$ compounds, the implementation of the tetragonal $I\bar{4}m2$ LT phase and the cubic $F\bar{4}3m$ HT phase yielded the most satisfying results. Our model consists of using two different Rb positions in each phase, which is in agreement with the analysis reported by Moritomo et al.[42] and is summarized in Table 2. We used the same relative Rb^+ occupancies for both phases, namely 92.1% for Rb position 1 and 7.9% for alternative Rb position 2. Because our samples contain varying amounts of lattice water molecules, these have been included in the fitting procedure according to Margadonna et al.[49] Following their method used for the nonstoichiometric $Rb_{0.7}Mn_{1.15}[Fe(CN)_6]\cdot 2H_2O$ material, we placed the O atoms of the H_2O molecules at positions where $Fe(CN)_6$ deficiencies occur, i.e., the O atom takes the place of the missing N cyanide atom. This means that on the N position, x N atoms and $1 - x$ O atoms were placed (see also Figure 1 and Table 2). The remaining water O atoms were placed in a similar fashion on tetrahedral

Table 2. Summary of Atomic Positions and Occupancy Factors for $Rb_xMn[Fe(CN)_6]_y\cdot zH_2O$ as Used in the Refinement of X-ray Powder-Diffraction Data[a]

	x	*y*	*z*	occupancy
		HT phase ($F\bar{4}3m$, Z=4)		
Fe	0	0	0	*y*
Mn	0.5	0.5	0.5	1
Rb1	0.25	0.25	0.25	0.921*x*
Rb2	0.75	0.75	0.75	0.079*x*
C	0.2054	0	0	*y*
N	0.3095	0	0	*y*
O1	0.25	0.25	0.25	$1 - 0.921x$
O2	0.75	0.75	0.75	$1 - 0.079x$
O3	0.3095	0	0	$1 - y$
		LT phase ($I\bar{4}m2$, $Z = 2$)		
Fe	0	0	0	*y*
Mn	0	0	0.5	1
Rb1	0	0.5	0.25	0.921*x*
Rb2	0	0.5	0.75	0.079*x*
C1	0	0	0.180	*y*
C2	0.200	0.200	0	*y*
N1	0	0	0.285	*y*
N2	0.311	0.311	0	*y*
O1	0	0.5	0.25	$1 - 0.921x$
O2	0	0.5	0.75	$1-0.079x$
O3	0	0	0.285	$1 - y$
O4	0.311	0.311	0	$1 - y$

[a] Positions from Moritomo et al.[42]

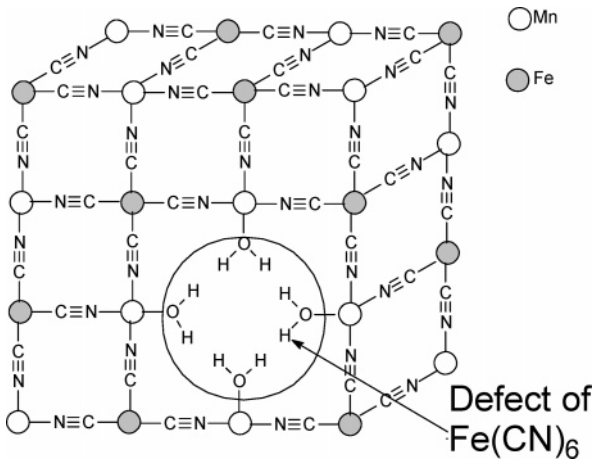

Figure 1. Visualization of an $Fe(CN)_6$ defect in the three-dimensional Prussian Blue-type lattice of $Rb_xMn[Fe(CN)_6]_y\cdot zH_2O$. Rb^+ ions and noncoordinated lattice water molecules are omitted for clarity.

(59) Osawa, H.; Iwazumi, T.; Tokoro, H.; Ohkoshi, S.-I.; Hashimoto, K.; Shoji, H.; Hirai, E.; Nakamura, T.; Nanao, S.; Isozumi, Y. *Solid State Commun.* **2003**, *125*, 237.
(60) Tokoro, H.; Ohkoshi, S.-I.; Matsuda, T.; Hozumi, T.; Hashimoto, K. *Chem. Phys. Lett.* **2004**, *388*, 379.
(61) Umekawa, M.; Hamada, N.; Kodama, A.; Moritomo, Y. *J. Phys. Soc. Jpn.* **2004**, *73*, 430.

Table 3. Selected X-ray Powder-Diffraction Data for $Rb_xMn[Fe(CN)_6]_y \cdot zH_2O$[a]

sample[b]	HT lattice constant a[c] (Å)	LT lattice constant a[c] (Å)	LT lattice constant c (Å)	%HT	%LT	R_{wp}[d]	R_{exp}[e]	GOF[f]
1	10.56	7.29	10.47	92.5	7.5	21.697	7.540	2.88
2	10.56	7.30	10.53	87.7	12.3	23.481	7.450	3.15
3	10.56	7.28	10.63	91.1	8.9	29.707	7.241	4.10
4	10.56	7.29	10.66	94.2	5.8	21.844	7.476	2.92

[a] The error for the lattice constants is ±0.1 Å and the error for the percentages of the relative contributions of the structures is ±0.5%. [b] Sample 1, $Rb_{0.59}Mn[Fe(CN)_6]_{0.86} \cdot 2.63H_2O$; sample 2, $(Rb_{0.92}Mn[Fe(CN)_6]_{0.95} \cdot 1.03H_2O)$; sample 3, $(Rb_{0.97}Mn[Fe(CN)_6]_{0.98} \cdot 1.03H_2O)$; and sample 4, $(Rb_{0.81}Mn[Fe(CN)_6]_{0.95} \cdot 1.24H_2O)$. [c] HT stands for the high-temperature phase $F\bar{4}3m$, LT for the low-temperature phase $I4m2$. [d] Weighted profile R value, $R_{wp} = \{\sum_i w_i[y_i(\text{obs}) - y_i(\text{calcd})]^2/\sum_i w_i[y_i(\text{obs})]^2\}^{1/2}$ with $y_i(\text{obs})$ = observed intensity, $y_i(\text{calcd})$ = calculated intensity, and w_i = weight. R_{wp} should be as close as possible to R_{exp}. [e] Statistical expected R value, $R_{exp} = [(N - P)/\sum_i^N w_i y_i(\text{obs})^2]^{1/2}$ with N = number of observations and P = number of parameters. R_{exp} should be as low as possible. [f] Goodness of fit, GOF = R_{wp}/R_{exp}; this value should be close to 1.

interstitial positions within the 3D framework where Rb^+ vacancies occur.

From the Rietveld analysis of the X-ray powder data, it becomes evident that all samples contain both the HT and LT phase to varying degrees. The extent to which the HT phase is present at room temperature has been found to be 87.7% for sample 2, 91.1% for sample 3, 92.5% for sample 1, and 94.2% for sample 4.

Although our fitting procedure allows us to obtain an estimate of the relative contributions of both the HT and LT phase in our samples at room temperature (Table 3), it is, however, to be noted that agreement with the recorded spectra may be considered as being rather poor. The origin for this lies in the present X-ray diffraction profiles having been recorded on a conventional X-ray powder diffraction setup, yielding, of course, less-accurate data compared to those obtained from an X-ray synchrotron-radiation source as used in the other studies. In addition, the present investigation is even more challenging than those reported previously in that the present fitting procedure includes the coexistence of both the LT and HT phase. In that respect, the results of our attempt to model these diffraction data may be considered quite reasonable. To a certain extent, it may be unanticipated that the fitting of X-ray powder data on such mixed-phase materials would yield such relatively reliable results, as the occurrence of two phases might involve boundaries or cross sections within the crystallites where the structure could be rather disordered. It may well be that the change from the HT to LT phase within these materials might occur in a relatively smooth fashion, as it involves only the elongation of one of the cubic axes to yield the tetragonal space group. This elongation may be quite subtle and could proceed gradually, i.e., no precise domains with one phase or the other need to be present.

Vibrational Spectroscopy. Spectroscopic investigation of compounds 1−4 was carried out in the spectral window 2000−2300 cm^{-1}, i.e., in the vicinity of the CN stretching mode, which is a fingerprint of structural and electronic changes occurring in Prussian Blue analogues. The CN stretching frequency of a free CN^- ion in aqueous solution is 2080 cm^{-1}, whereas upon coordination to a metal ion, it shifts to higher frequencies.[62]

The FTIR spectra, of which a representative example is shown in Figure 2, all show characteristic absorption bands

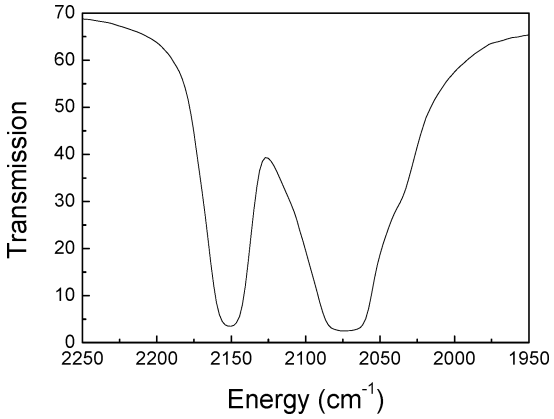

Figure 2. Room-temperature FTIR spectrum for $Rb_{0.59}Mn[Fe(CN)_6]_{0.86} \cdot 2.63H_2O$ (sample 1).

Table 4. FTIR Spectroscopic Data (CN stretching bands) for $Rb_xMn[Fe(CN)_6]_y \cdot zH_2O$

sample	position (fwhm)[a] of band 1 (cm^{-1})	position (fwhm)[a] of band 2 (cm^{-1})
1	2151 (34)	2074 (82)
2	2153 (15)	2101[b](91)
3		2101 (88)
4	2153 (18)	2090[c](108)

[a] Full width at half maximum. [b] Absorption at 2101 cm^{-1} and shoulder at 2070 cm^{-1}. [c] Superposition of an absorption at 2101 cm^{-1} and at 2079 cm^{-1}.

in the CN stretching region. The positions and line widths of these absorptions are listed in Table 4.

Assignments are based on literature data. From a comparative analysis of CN stretching vibrations for various $Fe(CN)_6$ and $Mn(CN)_6$ derivatives, it was concluded that the position of the υ_{CN} vibration appears to be considerably more sensitive to the C-bound metal ion and its oxidation state than it is to the N-bound metal ion and its valence state.[63] This is also the case for cyanide groups, establishing a linkage between two different metal ions in varying valence states.[64]

In fact, the absorption around 2150 cm^{-1} was assigned to the stretching of the CN ligand bridged between Fe^{III} and Mn^{II} ($Fe^{III}-CN-Mn^{II}$), whereas the absorption around 2095 cm^{-1} was assigned to the CN ligand, establishing a linkage between Fe^{II} and Mn^{III} ($Fe^{II}-CN-Mn^{III}$).[40,45,47] Depending on the extent of electron transfer that has occurred, both the high-temperature (high-spin Mn^{II} and low-spin Fe^{III}) and low-

(62) Nakamoto, K. In *Spectra of Inorganic and Coordination Compounds*, 4th ed.; Wiley: New York, 1986.

(63) Buschmann, W. E.; Ensling, J.; Gütlich, P.; Miller, J. S. *Chem.—Eur. J.* **1999**, *5*, 3019.

(64) Sato, O.; Einaga, Y.; Fujishima, A.; Hashimoto, K. *Inorg. Chem.* **1999**, *38*, 4405.

temperature (high-spin Mn^{III} and low-spin Fe^{II}) electronic configurations may be present at room temperature.[40]

Following this procedure, we may interpret the spectra of the present materials by assigning absorption 1 and 2 to the CN stretching vibration of $Fe^{III}-CN-Mn^{II}$ and $Fe^{II}-CN-Mn^{III}$, respectively. It is interesting to note that the position of cyano stretching vibration 1 remains virtually unaltered throughout the series and its position is in agreement with the assignment mentioned above, whereas the position of vibration 2 seems to reveal a dependence on the composition of the sample. In fact, the IR data of samples 2, 3, and 4 with lattice water contents close to 1 show a close similarity with the IR spectroscopic results reported for $RbMn[Fe(CN)_6]$[40,45,47] in that they exhibit a rather sharp absorption at around 2150 cm^{-1} together with a relatively broad band at about 2100 cm^{-1}. This latter absorption, originating from the $Fe^{II}-CN-Mn^{III}$ entity, is present as a single line for sample 3, whereas a distinct shoulder or slight splitting is observed for samples 2 and 4, respectively.

The close-to-2.6-fold hydrated sample 1 also displays a sharp peak at about 2150 cm^{-1} (vibration 1), but vibration 2 now occurs at a much lower frequency (2074 cm^{-1}). This shift to lower energy would be consistent with a weakening of the CN bond, implying that increased hydration of the material might involve a slight elongation of the CN linkage within the $Fe^{II}-CN-Mn^{III}$ framework.

Unfortunately, an assignment of the observed vibrational bands in terms of specific vibrational modes that are assigned purely on the basis of group theory considerations is severely hampered by the nonstoichiometric nature of the materials. The presence of water molecules, different sites for the Rb^+ ions, defects such as missing $Fe(CN)_6$ units, etc., eventually lead to a lowering of the local symmetry. This is true for both the IR and Raman data.

In contrast to IR absorption spectra, Raman spectra are not obscured by water lines, which gives a cleaner access to specific molecular vibrations. Raman spectra of the studied compounds in the spectral region 2000−2300 cm^{-1} are dominated by two strong Raman bands that are centered in the vicinity of 2165 cm^{-1} and 2156 cm^{-1} (see Figure 3). In addition, a rather weak Raman band (~5% of the total amplitude) is found around 2080 cm^{-1}. Between 2080 cm^{-1} and 2156 cm^{-1}, an irregular background is observed for some samples. The measured Raman spectra can be interpreted in analogy with the IR absorption data,[40] where the CN stretching mode corresponding to the IR band centered around 2150 cm^{-1} is attributed to CN ligands linking Fe^{III} and Mn^{II} ions, whereas the broad IR band centered around 2095 cm^{-1} is assigned to CN ligands located between Fe^{II} and Mn^{III} ions.

In Table 5, the constants obtained by multi-Lorentzian fitting of the Raman spectra depicted in Figure 3 are presented. Sample 1 exhibits noticeably broader Raman bands and the largest amount of "irregular background", whereas the fit parameters obtained for samples 2−4 are similar. Presumably the variations in relative intensities and width of bands 1 and 2 for sample 1 are due to its increased deviation from a perfect $RbMn[Fe(CN)_6]$ stoichiometry and associated larger water content. The activation of vibrational

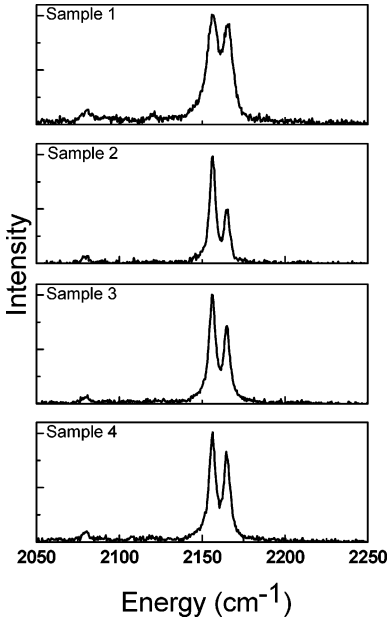

Figure 3. Room-temperature Raman spectra of samples 1 ($Rb_{0.59}Mn[Fe(CN)_6]_{0.86}\cdot 2.63H_2O$), 2 ($Rb_{0.92}Mn[Fe(CN)_6]_{0.95}\cdot 1.03H_2O$), 3 ($Rb_{0.97}Mn[Fe(CN)_6]_{0.98}\cdot 1.03H_2O$), and 4 ($Rb_{0.81}Mn[Fe(CN)_6]_{0.95}\cdot 1.24H_2O$).

Table 5. Raman Spectroscopic Data (CN stretching bands) for $Rb_xMn[Fe(CN)_6]_y\cdot zH_2O$

sample	position (fwhm)[a] of band 1 (cm^{-1})	position (fwhm)[a] of band 2 (cm^{-1})	position (fwhm)[a] of band 3 (cm^{-1})
1	2165.7 (6.3)	2156.3 (8.5)	2080.6 (5.9)
2	2165.0 (3.6)	2156.3 (4.2)	2079.6 (4.6)
3	2165.0 (4.3)	2156.1 (4.8)	2080.1 (10.7)
4	2165.0 (4.5)	2156.1 (4.7)	2079.7 (4.4)

[a] Full width at half maximum.

modes by the lowering the local symmetry may give rise to various bands, resulting in the observed broadening of the Raman bands and the "irregular background".

^{57}Fe Mössbauer Spectroscopy. The ^{57}Fe Mössbauer spectra of the four samples recorded at 80 K are displayed in Figure 4. The fit parameters are shown in Table 6. The experimental data were analyzed with two subcomponents, one singlet (site 1) and one doublet (site 2). The singlet corresponds to low-spin Fe^{II} ($S = 0$) ions situated in a symmetrical octahedral coordination sphere of CN ligands and the doublet to low-spin Fe^{III} ($S = 1/2$) ions. The values of the hyperfine parameters are in agreement with those reported in the literature.[64,65] Mössbauer parameters, isomer shift (δ), and quadrupole splitting (ΔE_q) of the iron in the structure unit $Fe(CN)_6$ are practically independent of the outer cations. The strongly bonded CN ligands effectively shield the iron atom from the outer environment, and the iron atom adopts a low-spin configuration in both valence states.

In all measurements, the samples were slowly cooled to 80 K, and no difference was observed in the spectra when the samples were immersed in liquid nitrogen and then transferred to the Mössbauer cryostat.

The spectrum recorded for sample 1 at 80 K consists of a superposition of the low-spin Fe^{II} singlet and the low-spin Fe^{III} doublet that both have the same isomer shift. The area

(65) Greenwood, N. N.; Gibb, T. C. In *Mössbauer Spectroscopy*; Chapman and Hall: London, 1971.

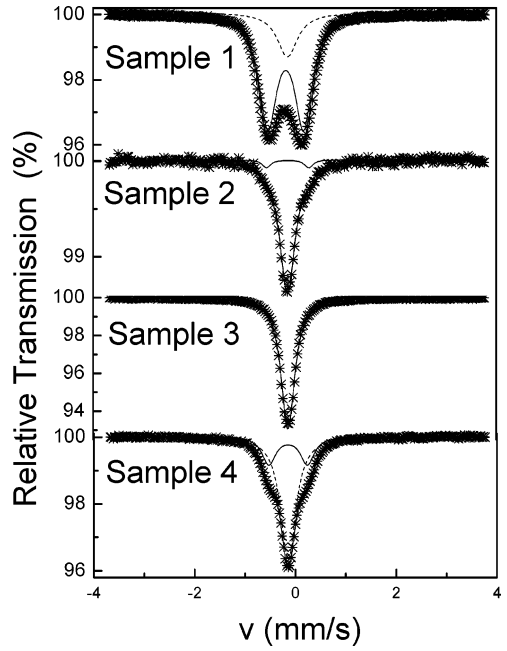

Figure 4. ^{57}Fe Mössbauer spectra recorded at 80 K for samples 1 ($Rb_{0.59}Mn[Fe(CN)_6]_{0.86}\cdot 2.63H_2O$),e 2 ($Rb_{0.92}Mn[Fe(CN)_6]_{0.95}\cdot 1.03H_2O$), 3 ($Rb_{0.97}Mn[Fe(CN)_6]_{0.98}\cdot 1.03H_2O$), and 4 ($Rb_{0.81}Mn[Fe(CN)_6]_{0.95}\cdot 1.24H_2O$).

fractions of the resonance lines are 19 ± 3% for Fe^{II} and 81 ± 3% for Fe^{III}, which is in agreement with the magnetic data (see below) showing that the material mainly consists of the HT configuration and does not exhibit any temperature-dependent electron-transfer process upon cooling. The broadness of the spectral features deserves particular attention, as the relatively large line widths could be assigned to the presence of attached Mn ions, which vary in their valence states and also in geometry: Mn^{II} about O_h and Mn^{III} about D_{4h} (Jahn−Teller distorted); this will give a range of slightly different Fe geometries.

The resonance lines for low-spin Fe^{II} and low-spin Fe^{III} are considerably broadened at 80 K. This feature, together with the superposition of the low-spin Fe^{II} and low-spin Fe^{III} resonance lines, will severely hamper the exact determination of the spectral contributions of both ions, particularly in those instances in which the spectral contribution of the low-spin Fe^{III} ions is relatively low. In fact, in the spectra recorded at 80 K, the signature for the low-spin Fe^{III} doublet can still be clearly distinguished for samples 2 and 4 in the form of shoulders at the outer parts of the overlapping low-spin Fe^{II} and low-spin Fe^{III} absorption lines. The spectral contribution of low-spin Fe^{III} can, therefore, with certainty be estimated to be on the order of 7 ± 3% for sample 2 and 29 ± 3% for sample 4. For sample 3, this characteristic feature on which the low-spin Fe^{III} contribution can be based is not clearly visible, because in this instance it is entirely obscured by the broad single line originating from low-spin Fe^{II}. Hence, it cannot be excluded that low-spin Fe^{III} may contribute, to a minor extent, to the spectral density; however, its exact area fraction cannot be accurately determined, so there remains an uncertainty in the Fe^{III} percentage present at this temperature.

Magnetic Measurements. The magnetic behavior of the four samples is shown in Figure 5 in the form of $\chi_M T$ vs T plots, where χ_M is the molar magnetic susceptibility per formula unit and T is the temperature.

Assuming that the materials consist exclusively of either the LT or HT phase and taking a g value equal to 2, we calculate that the theoretical $\chi_M T$ values would amount to 3.01 cm^3 K mol^{-1} for an $\{S_1;S_2\} = \{2;0\}$ system (high-spin Mn^{III} and low-spin Fe^{II}) and 6.01 cm^3 K mol^{-1} for an $\{S_1;S_2\} = \{5/2;1/2\}$ system (high-spin Mn^{II} and low-spin Fe^{III}). These values have not been found experimentally, as all materials contain both LT and HT configuration to various extents at all temperatures, resulting in an underestimation of the $\chi_M T$ value for temperatures at which the HT configuration is expected and an overestimation of these values when the LT configuration is expected. Second, all $Rb_xMn[Fe(CN)_6]_y\cdot zH_2O$ materials show significant, although different, deviations from the perfect Rb:Mn:Fe stoichiometry of 1:1:1. At the extremes of the magnetic curves, a major fraction of the sample (denoted by y) is then either formed by an $\{S_1;S_2\} = \{2;0\}$ system (high-spin Mn^{III} and low-spin Fe^{II}) or an $\{S_1:S_2\} = \{5/2;1/2\}$ system (high-spin Mn^{II} and low-spin Fe^{III}), whereas a minor fraction (given by $1 - y$) is represented by nonmagnetically coupled $Mn(NC)_6$ entities, which most probably contain high-spin Mn^{II} ions ($S = 5/2$). This has the effect of underestimating the $\chi_M T$ value at temperatures for which the HT configuration is expected, whereas an overestimation of this value occurs at temperatures for which the LT configuration is expected.

The $\chi_M T$ vs T curve for sample 1 ($Rb_{0.59}Mn[Fe(CN)_6]_{0.86}\cdot 2.63H_2O$) indicates that it does not exhibit a conversion from the high-temperature to the low-temperature configuration. To the best of our knowledge, this is the first sample belonging to the family of $Rb_xMn[Fe(CN)_6]_y\cdot zH_2O$ compounds that does not show the temperature-induced interconversion between the high- and low-temperature configurations.

The $\chi_M T$ value at high temperature, 4.07 cm^3 K mol^{-1}, is significantly lower than the $\chi_M T$ value of 6.01 cm^3 K mol^{-1} (calculated for $g = 2$) that would be expected for a complete population of the HT configuration. This feature can be explained by the observed significant lack (14%) of $Fe(CN)_6$ entities and the presence of a relatively small fraction of LT configuration. The presence of such a minor portion consisting of high-spin Mn^{III} ($S = 2$) and low-spin Fe^{II} ($S = 0$) is in agreement with the results of various types of spectroscopic measurements reported in the present paper.

The existence of a small amount of the LT phase can also be inferred from the $\chi_M T$ behavior at low temperature. In this temperature range, the occurrence of a peak in the $\chi_M T$ curve is due to the superposition of a signal due to the ferromagnetic ordering of the residual LT phase and due to the predominant $\chi_M T$ signal of the HT phase exhibiting a paramagnetic behavior.

The data for sample 2 recorded during heating from 5 to 350 K first show a decrease in $\chi_M T$ until it reaches the value of 3.1 cm^3 K mol^{-1} at 255 K; it then increases sharply to a value of 4.5 cm^3 K mol^{-1} at 300 K. Upon the sample being cooled, the $\chi_M T$ value abruptly decreases at 242 K to reach a value of 3.1 cm^3 K mol^{-1} at 195 K. A thermal hysteresis width of 52 K characterized by $T_{1/2}{\downarrow} = 234$ K and $T_{1/2}{\uparrow} =$

Table 6. ^{57}Fe Mössbauer Parameters Resulting from Least-Squares Fits of the 80 K Spectra of $Rb_xMn[Fe(CN)_6]_y \cdot zH_2O$[a]

	site 1				site 2			
sample	δ_{Fe} (mm/s)	ΔE_q (mm/s)	Γ (mm/s)	area (%)	δ_{Fe} (mm/s)	ΔE_q (mm/s)	Γ (mm/s)	area (%)
1	−0.04	0.00	0.48	19	−0.08	0.71	0.42	81
2	−0.04	0.00	0.37	93	−0.04	0.84	0.21	7
3	−0.03	0.00	0.32	100				
4	−0.04	0.00	0.36	71	−0.05	0.76	0.33	29

[a] The most probable error for the hyperfine parameters is ±0.01 mm s^{-1} and for the area is ±3%.

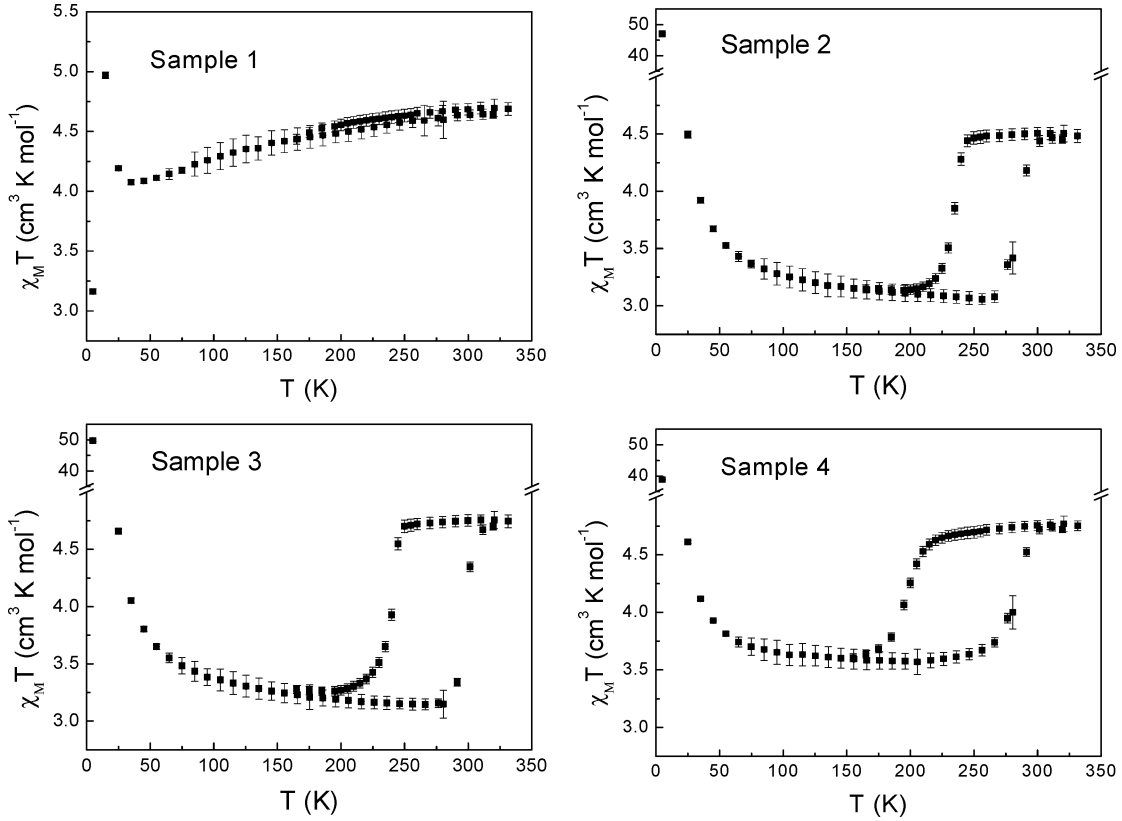

Figure 5. Temperature dependence of $\chi_M T$ for samples 1 ($Rb_{0.59}Mn[Fe(CN)_6]_{0.86} \cdot 2.63H_2O$), 2 ($Rb_{0.92}Mn[Fe(CN)_6]_{0.95} \cdot 1.03H_2O$), 3 ($Rb_{0.97}Mn[Fe(CN)_6]_{0.98} \cdot 1.03H_2O$), and sample 4 ($Rb_{0.81}Mn[Fe(CN)_6]_{0.95} \cdot 1.24H_2O$)

286 K has been detected. The $\chi_M T$ vs T plot for sample 3 has a fairly similar shape; however, the hysteresis width has increased to 57 K ($T_{1/2}\downarrow$ = 240 K, $T_{1/2}\uparrow$ = 297 K). The limiting values for $\chi_M T$ encompassing this hysteresis loop are 3.2 cm^3 K mol^{-1} at 277 K and 4.8 cm^3 K mol^{-1} at 333 K.

Sample 4 exhibits a much broader hysteresis (width 86 K, $T_{1/2}\downarrow$ = 197 K, $T_{1/2}\uparrow$ = 283 K). In addition, the value of $\chi_M T$ for the LT phase is significantly higher (3.6 cm^3 K mol^{-1}), whereas that for the HT phase is on a similar order (4.8 cm^3 K mol^{-1}).

The magnetic behavior of the electron-transfer active compounds is comparable to that reported for RbMn[Fe(CN)$_6$], which displays a thermal hysteresis width of 73 K ($T_{1/2}\downarrow$ = 231 K, $T_{1/2}\uparrow$ = 304 K).[41] The limiting values for this hysteresis loop in $\chi_M T$ are 3.2 cm^3 K mol^{-1} at 200 K and 4.7 cm^3 K mol^{-1} at 320 K.

Examining these $\chi_M T$ values while taking into account that these samples are somewhat short in spin-carrying Fe(CN)$_6$ entities leads to the conclusion that the temperature-induced switching process is incomplete in all instances, with the extent of the electron transfer being the largest for sample 3. All compounds show the general feature that the residual HT fraction present at low temperatures appears to be larger than the residual LT fraction at higher temperatures.

Figure 6 shows the magnetization vs temperature curves of the four samples. Sample 1 does not show any significant magnetization, but samples 2, 3, and 4 do exhibit spontaneous magnetization below T_c = 12 K. The order of the magnetization decreases from sample 3 to 2 to 4. The ordering temperature of 12 K corresponds exactly to what has been reported for RbMn[Fe(CN)$_6$].[45]

The magnitude of the magnetization is determined by the extent to which the LT phase (the $\{S_1;S_2\} = \{2;0\}$ system consisting of high-spin Mn^{III} and low-spin Fe^{II}) is present at low temperatures. The ^{57}Fe Mössbauer data recorded at 80 K give valuable information in that the spectral contribution of low-spin Fe^{II} varies with increasing magnetization values, yielding 100% for sample 3, 93% for sample 2, and only 71% of low-spin Fe^{II} ions for sample 4. An assessment of the contribution of this LT electronic configuration on the basis of the $\chi_M T$ value determined at temperatures below the thermal hysteresis feature is hampered by the face that it also consists of a fraction of residual HT electronic configuration and a small percentage of high-spin Mn^{II} ions. Both of these factors lead to the observation of a $\chi_M T$ value

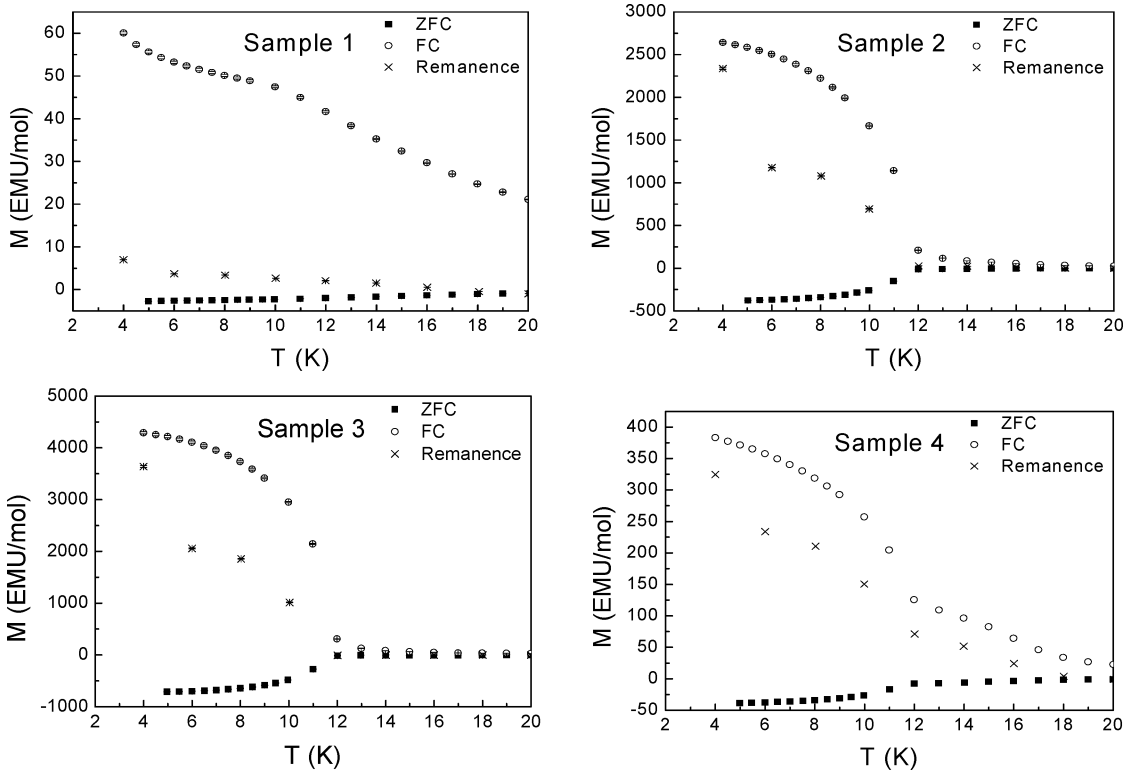

Figure 6. Temperature dependence of the magnetization for samples 1 ($Rb_{0.59}Mn[Fe(CN)_6]_{0.86} \cdot 2.63H_2O$), 2 ($Rb_{0.92}Mn[Fe(CN)_6]_{0.95} \cdot 1.03H_2O$), 3 ($Rb_{0.97}Mn[Fe(CN)_6]_{0.98} \cdot 1.03H_2O$), and 4 ($Rb_{0.81}Mn[Fe(CN)_6]_{0.95} \cdot 1.24H_2O$). Notice the differences in the scale of the *y*-axis. ZFC = zero-field cooled, FC = field cooled.

that will be higher than expected for a pure LT configuration; however, an analysis may be given the focuses on getting access to these various contributions to $\chi_M T$. The amount of high-spin Mn^{II} ions is proportional to the number of $Fe(CN)_6$ defects present in the various $Rb_xMn[Fe(CN)_6] \cdot zH_2O$ compounds, hence its contribution may be expected to vary as $1 - y$. This leads to the conclusion that the correction for the Mn^{II} contribution will be the largest for sample 2 and 4, whereas it should be somewhat smaller for sample 3. The contribution arising from the residual HT configuration present at low temperatures may be estimated from the ^{57}Fe Mössbauer spectroscopic data recorded at 80 K, which show that the low-spin Fe^{III} content, which is indicative of the fraction of HT phase present, varies from sample 3 (0%) to sample 2 (7%) to sample 4 (29%). Therefore, access to purely LT configuration-based $\chi_M T$ values would simply imply a larger correction factor for sample 4 than for sample 2 and 3, respectively. In view of this analysis, the observed $\chi_M T$ values for the various samples do indeed reflect the trend set out by the magnetization values.

The inverse magnetic susceptibility data from 15 to 265 K (not shown here) were fitted with a straight line yielding θ values of 9.0 ± 0.2 K, 9.6 ± 0.2 K, and 3.2 ± 1.1 K for samples 2, 3, and 4, respectively. From the $\chi_M T$ values at the lower limit of the hysteresis loops, as well as from the ^{57}Fe Mössbauer spectroscopic data recorded at 80 K, it is evident that sample 2 and 3 contain relatively small amounts of the HT configuration, whereas sample 4 contains a far larger percentage of this configuration. In the determination of the θ values, an increasing amount of the HT configuration will result in an underestimation of the ferromagnetic coupling. Despite this inaccuracy in the θ values, it can still be safely concluded that a weak ferromagnetic coupling occurs between neighboring metal ions in the LT phase. This ferromagnetic exchange coupling in the LT phase has been proposed to arise from a mechanism of mixed-valence electron delocalization of the Mn ions, similar to what was reported for the Fe^{III} ions in Prussian Blue $Fe^{III}_4[Fe^{II}(CN)_6]_3 \cdot 14H_2O$.[40,66]

X-ray Photoelectron Spectroscopy (XPS). This technique is a direct method for identifying the oxidation states in compounds and giving quantitative information about the elemental composition of the Prussian Blue analogues.[46,67] Figure 7 shows the survey spectrum of sample 2. As labeled in the spectrum, characteristic photoelectron and Auger peaks of Fe, Mn, C, N, Rb, and O are clearly distinguishable. We now discuss the different spectral regions corresponding to the various elements separately. Figure 8 shows the XP spectrum of the whole Fe 2p region (a) and a close-up on the Fe $2p_{3/2}$ region (b) for sample 2. The fit was obtained using a Tougaard background (Figure 8a) and Gaussian functions for each peak. The close-up of the Fe $2p_{3/2}$ peak (Figure 8b) demonstrates that it consists of three contributions: the Fe^{II} line at 708.5 eV binding energy, the Fe^{III} main line at 710.1 eV, and the satellite of Fe^{III} at 711.7 eV, 1.6 eV higher binding energy than that of the main peak, with an intensity 0.22 times that of the main peak.[68] We can therefore compute the ratio of Fe^{II}:/Fe^{III} in sample 2 from the relative intensities of the photoemission lines and obtain

(66) Mayoh, B.; Day, P. *J. Chem. Soc., Dalton Trans.* **1976**, 1483.
(67) Sauter, S.; Wittstock, G.; Szargan, R. *Phys. Chem. Chem. Phys.* **2001**, *3*, 562.
(68) Oku, M.; Wagatsuma, K.; Konishi, T. *J. Electron Spectrosc. Relat. Phenom.* **1999**, *99*, 277.

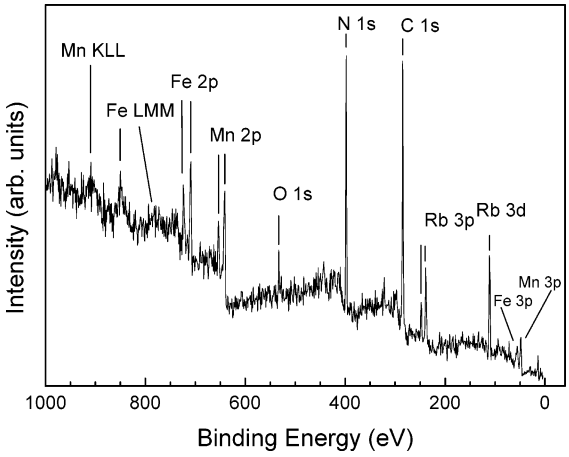

Figure 7. X-ray photoemission survey spectrum of sample 2 ($Rb_{0.92}Mn[Fe(CN)_6]_{0.95}\cdot 1.03H_2O$). Photoemission and Auger lines are labeled.

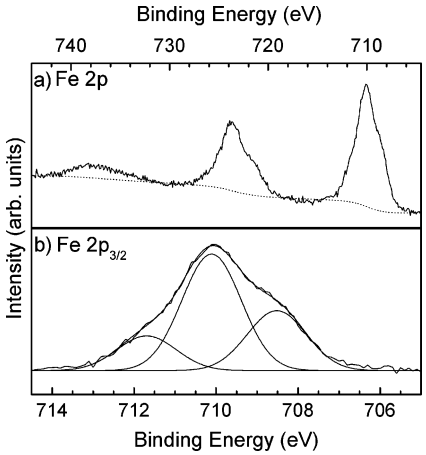

Figure 8. (a) X-ray photoemission spectrum of sample 2 ($Rb_{0.92}Mn[Fe(CN)_6]_{0.95}\cdot 1.03H_2O$) and (b) close-up of the Fe $2p_{3/2}$ region after background subtraction. The fit was performed using a Tougaard background and Gaussian functions for each peak.

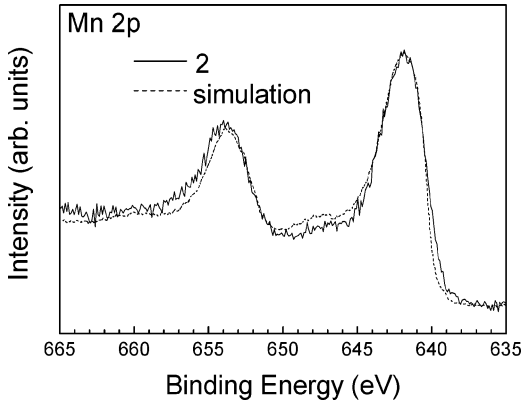

Figure 9. X-ray photoemission spectrum of the Mn 2p region for sample 2 ($Rb_{0.92}Mn[Fe(CN)_6]_{0.95}\cdot 1.03H_2O$). The simulated spectrum was generated from the MnO and Mn_2O_3 signals[68] multiplied by the respective percentages of Fe^{III} and Fe^{II} determined for the same sample (for details, see text).

69% Fe^{III} and 31% Fe^{II}. Consequently, the Mn 2p spectra should present spectral features representative of 69% Mn^{II} and 31% Mn^{III}. Figure 9 represents the Mn 2p region of the XP spectrum. The two spin−orbit split contributions centered at 641.8 and 653.8 eV binding energy are both very broad because of multiplet splitting.[68−70] If we concentrate, as we did for Fe, on the $2p_{3/2}$ contribution, we notice that, according to the literature, the Mn^{II} and Mn^{III} peaks are expected at 641.8 and 642.5 eV, respectively.[46] However, with our XP resolution, we cannot separate these two lines. To verify that we indeed obtain the expected ratio between Mn^{II} and Mn^{III}, we therefore tried to simulate the spectrum starting from the MnO and Mn_2O_3 spectra reported in the literature[68] and multiplied them by the respective percentages of Fe^{III} and Fe^{II} quoted above. This procedure reproduces the experimental data very well (dashed line in Figure 9) except for an increase of 0.8 eV in the binding energy (compared to the value found in the literature for the manganese oxides), probably because of the different environment present in the rubidium manganese hexacyanoferrate compound. Thus, our spectral analysis is consistent with the coexistence of two electronic configurations in the sample, one containing Fe^{III} and Mn^{II} and the other containing Fe^{II} and Mn^{III}. Importantly, the XP spectral analysis confirms the presence of identical percentages of Mn^{II} and Fe^{III} or Mn^{III} and Fe^{II}. This would be in agreement with the presence of distinct LT and HT configurations. All samples were analyzed the same way, and the respective percentages of Fe^{III} are reported in Table 7 (see below).

Additionally, we checked the influence of exposure to daylight during the synthesis. The XP spectrum of Fe (Figure 10) of sample 4 prepared (and measured) in the dark still shows the presence of two components corresponding to Fe^{II} and Fe^{III} at the same binding energies as those for sample 2 exposed to white light during synthesis and XPS analysis.

Let us now briefly comment on rubidium. For all four samples, the Rb $3d_{5/2}$ XPS spectra (not shown) present a peak at 110.5 eV. In the Prussian Blue analogues, the rubidium atoms are noncoordinated in the tetrahedral sites (see Figure 1) and hence are similar to those in alkali intercalation compounds. This explains why we find a binding energy that coincides with that of Rb^+ intercalated in $TiSe_2$ and $TiTe_2$ layered materials. [71]

The O1s region of the photoemission spectra are shown in Figure 11 for all four samples. Four components are needed to reconstruct the spectral shape. The first two components are centered at 529.4 and 530.6 eV and represent the water coordinated to Mn^{III} and Mn^{II}, respectively, [72,73] i.e., in the absence of $Fe(CN)_6$ entities, the octahedral coordination about the manganese ions is completed by aqua ligands. The third component is centered at 532.1 eV binding energy and represents the unavoidable contamination of the samples because of exposure to air,[74] whereas the highest binding-energy component at 533.7 eV is due to the noncoordinated water molecules inside the Prussian Blue analogue samples.[75] The intensity of the peak corresponding to noncoordinated water in samples 1 and 2 is higher than that due to coordinated water, whereas the two intensities

(69) Oku, M.; Hirokawa, K.; Ikeda, S. *J. Electron Spectrosc. Relat. Phenom.* **1975**, *6*, 451.
(70) Oku, M.; Matsuta, H.; Wagatsuma, K. *J. Chem. Soc., Faraday Trans.* **1996**, *92*, 2759.
(71) Stoltz, S. E.; Starnberg, H. I.; Holleboom, L. J. *Phys. Rev. B* **2005**, *71*, 125403.
(72) Feliu, S.; Perez-Revenga, M. L. *Appl. Surf. Sci.* **2004**, *229*, 112.
(73) Katsoyiannis, I. A.; Zouboulis, A. I. *Water Res.* **2004**, *38*, 1992.
(74) Barr, T. L.; Yin, M. *J. Vac. Sci. Technol., A* **1992**, *10*, 2788.
(75) Andersson, K.; Nikitin, A.; Pettersson, L. G. M.; Nilsson, A.; Ogasawara, H. *Phys. Rev. Lett.* **2004**, *93*, 196101.

Table 7. Atomic Composition of the Samples as Deduced from XPS Analysis[a]

sample	Fe	Mn	Rb	N	O noncoordinated water molecules	O coordinated water molecules	Fe^{III} (%)
1	1.0 ± 0.1	1.0 ± 0.1	0.94 ± 0.05	6	0.47 ± 0.05	0.23 ± 0.03	60 ± 1
2	1.0 ± 0.1	1.0 ± 0.1	1.02 ± 0.05	6	0.50 ± 0.05	0.27 ± 0.03	69 ± 1
3	1.1 ± 0.1	1.0 ± 0.1	1.02 ± 0.05	6	0.25 ± 0.03	0.34 ± 0.04	76 ± 1
4	1.1 ± 0.1	1.1 ± 0.1	0.69 ± 0.03	6	0.16 ± 0.02	0.69 ± 0.05	75 ± 1

[a] The data are referenced to the nitrogen value, assumed to be 6. The error is 10 % for Mn and Fe and 5% for the remaining elements. The last column indicates the percentage of Fe atoms in the Fe^{III} oxidation state for each sample.

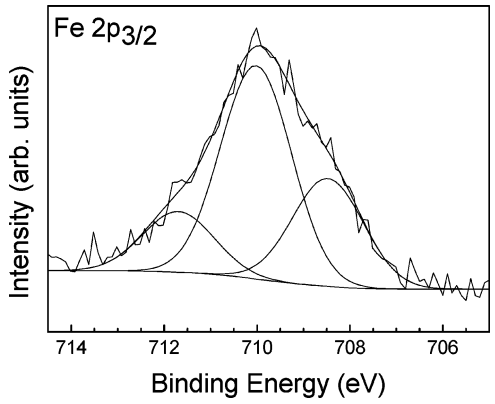

Figure 10. X-ray photoemission spectrum of the Fe $2p_{3/2}$ region for sample 4 ($Rb_{0.81}Mn[Fe(CN)_6]_{0.95} \cdot 1.24H_2O$) prepared in the dark.

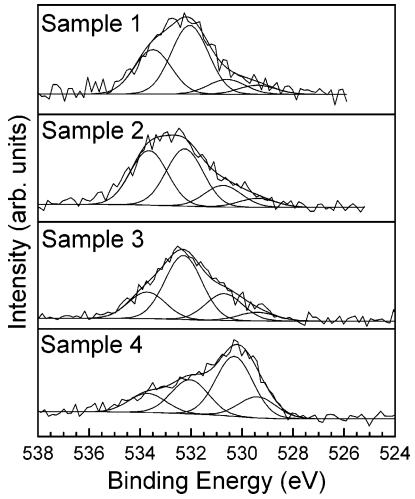

Figure 11. X-ray photoemission spectrum of the O 1s region for samples 1 ($Rb_{0.59}Mn[Fe(CN)_6]_{0.86} \cdot 2.63H_2O$), 2 ($Rb_{0.92}Mn[Fe(CN)_6]_{0.95} \cdot 1.03H_2O$), 3 ($Rb_{0.97}Mn[Fe(CN)_6]_{0.98} \cdot 1.03H_2O$), and 4 ($Rb_{0.81}Mn[Fe(CN)_6]_{0.95} \cdot 1.24H_2O$).

are comparable in sample 3. In sample 4, the intensity of the peak corresponding to coordinated water is instead higher than that of noncoordinated water. This means that samples 1 and 2 contain a higher amount of noncoordinated water compared to water at defects, whereas in sample 4, the situation is reversed. In sample 3, the amount of noncoordinated water molecules is equal to the number of the defects. The relative atomic percentages of oxygen from coordinated and noncoordinated water determined from the O1s peak areas are reported in Table 7.

If we now compare the elemental composition of the samples deduced from the X-ray photoemission peak areas reported in Table 7 (C has been excluded from this analysis because a small amount of contamination is always present at the surface of these air-exposed samples.[76]), we note a slight disagreement between the stoichiometric formula obtained by elemental analysis and the atomic percentages deduced from XPS measurements. These differences can be attributed to the fact that elemental analysis is a bulk sensitive technique, whereas XPS is a surface probe. In addition, because XPS has to be performed in ultrahigh vacuum, the samples lose water from the surface of the sample.

Conclusion

The compounds of general formula $Rb_xMn[Fe(CN)_6]_y \cdot zH_2O$ clearly represent an intriguing class of compounds. The obtained compositions of the $Rb_xMn[Fe(CN)_6]_y \cdot zH_2O$ compounds in terms of their differing in stoichiometry and water content may be explained by the variation in the synthetic procedures involved. Complexation of Mn^{II} and $Fe^{III}(CN)_6$ is extremely fast and irreversible, as can be seen from the instantaneous precipitation of the material when two solutions containing each ingredient are added together. Therefore, concentration effects are extremely important in determining the nature of the product formed. So when we start with a solution of $MnCl_2 \cdot 4H_2O$ and add $K_3Fe(CN)_6$ (as in sample 1), the Mn^{II} concentration is high at the initial stages of the precipitation and $Fe^{III}(CN)_6$ defects will be formed within the material. Instead of N-donating $Fe^{III}(CN)_6$ entities, water molecules will complete the presumably still octahedral coordination about the Mn^{II} ion. On the contrary, when the solutions are added in a reverse order (as in sample 2), fewer $Fe^{III}(CN)_6$ defects will be formed. When the solutions are added simultaneously (sample 3), the product formation process shows little difference compared to the one in which $MnCl_2 \cdot 4H_2O$ is added to $K_3Fe(CN)_6$.

From the results reported previously,[32,41−46,58−60] one could have concluded that single-phase materials had exclusively been obtained and that the solid-state material would undergo an electron-transfer process that enabled the interconversion between the so-called high-temperature (high-spin Mn^{II} and low-spin Fe^{III}) and low-temperature (high-spin Mn^{III} and low-spin Fe^{II}) phases. This transformation is accompanied by a change from cubic to tetragonal symmetry, which is associated with the Jahn−Teller distortion of the Mn^{III} center. Our results point to the direction that these redox processes do occur in a much more subtle way and can, to a certain extent, be controlled during the synthesis, where concentration effects may have a paramount influence on the nature of the resulting solid state material. In fact, it may be concluded that redox processes have occurred to varying extents during the synthesis and this is confirmed by all solid compounds containing both LT and HT configuration to varying degrees at room temperature. The HT phase clearly predominates at

(76) Barr, T. L. In *Practical Surface Analysis*; Briggs, D., Seah, M. P., Eds; John Wiley & Sons: Chinchester, U.K., 1990. .

this temperature, as indicated by the relatively high $\chi_M T$ values obtained for all compounds at room temperature. From the evolution of these $\chi_M T$ values, we may estimate that the fraction of LT configuration present decreases in the range from sample 2 to sample 3 to sample 4 to sample 1. Although the relative contributions of both phases obtained from the X-ray powder-diffraction study may not be considered as being extremely accurate, this trend is also found: the apparent reversal of sample 4 and 1 in this sequence may have its reason in the experimental error associated with this experimental procedure. The IR spectroscopic data also agree with the trend mentioned above, in that the higher-frequency absorption 2 attributed to the $Fe^{II}-CN-Mn^{III}$ cyano linkage present in the LT phase is displaced toward lower energy as the relative contribution of this electronic configuration increases from samples 2 and 3 to sample 4 to sample 1. Also, the Raman data agree with this series, in that the relative contribution of the band located at 2165 cm^{-1} increases in going from sample 2 to sample 3 to sample 4 to sample 1. The same trend is observed for the band at 2080 cm^{-1}.

The XPS experiments have been very valuable in having yielded direct evidence for the coexistence of identical percentages of Fe and Mn ions in oppositely matching oxidation states, in agreement with the presence of the Fe^{II}-Mn^{III} LT and the $Fe^{III}Mn^{II}$ HT electronic configurations. Importantly, this information suggests that the redox processes operating within these materials involve only electron transfer from Mn to Fe and vice versa, concomitant with the proposed electron-transfer mechanism.

The magnetic data for the electron-transfer-active compounds show a unique trend, with the LT configuration content at room temperature increasing from sample 4 to sample 3 to sample 2. Sample 4, which contains the LT electronic configuration to a lesser extent, appears to exhibit the broadest hysteresis (86 K), whereas the thermal hysteresis width diminishes considerably with increasing fraction of the LT configuration, yielding 57 K for sample 3 and only 52 K for sample 2. Considering that the electron-transfer transitions during heating and cooling are first order in origin, the temperatures at half-maximum may be determined by the extent to which domains of nonactive electron-transfer entities are present in the sample. This may lead to a reduced cooperative behavior, which might be comparable to, for instance, metal dilution effects observed in Fe^{II} spin crossover compounds.[77−79]

Sample 1 represents the first example within the family of $Rb_xMn[Fe(CN)_6]_y \cdot zH_2O$ compounds of a material that does not exhibit the temperature-induced interconversion between the high- and low-temperature configurations. This difference in magnetic behavior compared to that of the other samples may be related to its composition, which shows the largest deviation from a perfect $RbMn[Fe(CN)_6]$ stoichiometry and an associated considerably larger number of lattice water molecules.

These factor seems to be the key toward explaining the observed difference in physical behavior of the samples. The closer a sample's Rb:Mn:Fe ratio is to 1:1:1, the less water is present. One water molecule is positioned at the Rb^+ vacancies. The remaining water molecules fill the positions of the $Fe(CN)_6$ defects, as depicted in Figure 1. The latter has the consequence that the Mn ions get more water molecules in their coordination shell, resulting in the formation of presumably still octahedral $Mn(NC)_{6-a}(H_2O)_a$ entities. The replacement of the relatively strong N-donating cyano ligands by the weaker aqua donors will lead to a significant lowering of the ligand field strength. Another important corollary of this is that the redox potential of the Mn entity will change dramatically, such that the close-to-stoichiometric compounds (sample 2, 3, and 4) containing the $Mn^{II}(NC)_6/Mn^{III}(NC)_6$ redox couple display electron-transfer behavior, whereas sample 1, which contains $Mn^{II}(NC)_{6-a}(H_2O)_a/Mn^{III}(NC)_{6-a}(H_2O)_a$, does not show any sign of the occurrence of electron-transfer processes.

Interestingly, both vibration spectroscopic techniques seem to be appropriate tools for rapid screening of the compounds, which allows for an indirect assessment of their aptness to undergo electron-transfer processes. Electron-transfer-inactive compounds are typically more hydrated and possess a concomitant larger deviation from perfect stoichiometry, which is reflected by the extent to which absorption 2 observed in the IR spectra ($Fe^{II}-CN-Mn^{III}$) is shifted to lower frequencies, as well as by the increase in intensity of Raman bands 1 and 3.

The magnetization vs temperature curves for the electron-transfer-active compounds show spontaneous magnetization below $T_c = 12$ K; the extent of this magnetization inversely correlates with the residual fraction of the HT electronic configuration present at lower temperatures. The ^{57}Fe Mössbauer spectroscopic data recorded at 80 K show that the low-spin Fe^{III} content, which is indicative of the fraction of the HT phase present, varies from sample 3 (0%) to sample 2 (7%) to sample 4 (29%). This increasing amount of residual HT configuration within the series correlates with the increased hydration of the samples. In fact, the electron-transfer-active materials contain two forms of HT electronic configurations at higher temperatures, i.e., redox-active $Mn^{II}(NC)_6$ entities, which are converted to the LT configuration on cooling, and redox-inactive $Mn^{II}(NC)_{6-a}(H_2O)_a$ chromophores, which are responsible for the residual HT fraction at low temperatures. The relative contribution of the latter is enhanced upon increased hydration of the samples.

This study has shown how small but significant variations in the composition of the materials may be obtained by modifications in the synthetic procedure. These reproducible adjustments of the molecular composition allow for the controlled tuning and optimization of the physical properties (the extent of magnetization and the thermal hysteresis width) associated with the metal-to-metal charge-transfer process within this family of $Rb_xMn[Fe(CN)_6]_y \cdot zH_2O$ Prussian Blue-type analogues.

(77) Jung, J.; Schmitt, G.; Wiehl, L.; Knorr, K.; Spiering, H.; Gütlich, P. *Z. Phys. B*, **1996**, *100*, 523.
(78) Martin, J.-P.; Zarembowitch, J.; Dworkin, A.; Haasnoot, J. G.; Codjovi, E. *Inorg. Chem.* **1994**, *33*, 2617.
(79) Martin, J.-P.; Zarembowitch, J.; Bousseksou, A.; Dworkin, A.; Haasnoot, J. G.; Varret, F. *Inorg. Chem.* **1994**, *33*, 6325.

Acknowledgment. The authors thank Mr. Jacob Baas and Ms. Mylène Sage for their assistance with the magnetic measurements and powder-diffraction profiles and Prof. Thomas Palstra and Prof. Bart Hessen for their interest in this research. This work is part of the research program of the Stichting voor Fundamenteel Onderzoek der Materie (FOM, financially supported by the Nederlandse Organisatie voor Wetenschappelijk Onderzoek (NWO)). Financial support for this work has also been provided by MSC_{plus}.

Supporting Information Available: Measured, calculated, and difference curves for the X-ray powder diagrams for samples 1, 2, 3, and 4 (pdf). This material is available free of charge via the Internet at http://pubs.acs.org.

CM052521X